

**1 Size-differentiated Export in Different Dynamical  
2 Regimes in the Ocean**

**3 M. Dever<sup>1</sup>, D. Nicholson<sup>1</sup>, M. M. Omand<sup>2</sup>, and A. Mahadevan<sup>1</sup>**

**4** <sup>1</sup>Woods Hole Oceanographic Institution, Woods Hole, MA 02543, USA

**5** <sup>2</sup>Graduate School of Oceanography, University of Rhode Island, Narragansett, Rhode Island, USA

**6 Key Points:**

- 7** • Submesoscale dynamics enhance the contribution of slow-sinking particles to  
**8** POC export, especially for steep particle size-spectrum slopes  
**9** • Remineralization processes intensify the role of slow-sinking particles, to the  
**10** point where these particle sometime dominate POC export

11      **Abstract**

12      Export of Particulate Organic Carbon (POC) is mainly driven by gravitational sinking.  
 13      Thus, traditionally, it is thought that larger, faster-sinking particles make up most of  
 14      the POC export flux. However, this need not be the case in a dynamic oceanic flow  
 15      field, where the ocean velocity can influence the descent rate of particles. Particles  
 16      with different settling speeds are released in two process-oriented model simulations  
 17      of an upper ocean eddying flow to evaluate the impact of (1) ocean dynamics on the  
 18      respective contribution of the different sinking-velocity classes to POC export, and  
 19      (2) the particle number size-spectrum slope. The analysis reveals that the leading  
 20      export mechanism changes from gravitationally-driven to advectively-driven as sub-  
 21      mesoscale dynamics become more important. The vertical velocity associated with  
 22      submesoscale dynamics enhances the contribution of slower-sinking particles to POC  
 23      export. A steeper particle size spectrum, also increases the relative contribution of  
 24      smaller, slower-sinking particles. Implementing a remineralization scheme generally  
 25      decreases the total amount of biomass exported, but its impact is weaker in dynamical  
 26      regimes where submesoscale dynamics are present and export is advectively-driven.  
 27      Under specific conditions, remineralization processes counter-intuitively enhance the  
 28      role of slower-sinking particles to the point where these slower-sinking velocity classes  
 29      dominate the export, therefore challenging the traditional paradigm for POC export.  
 30      This study demonstrates that slow-sinking particles can be a significant contribution,  
 31      and at times, even dominate the export flux.

32      **1 Introduction**

33      Photosynthesis in the sunlit upper ocean and the production of Particulate Or-  
 34      ganic Carbon (POC) takes up dissolved inorganic carbon and facilitates the uptake  
 35      of CO<sub>2</sub> from the atmosphere. The sinking of POC exports organic carbon from the  
 36      upper ocean to the interior, leading to the sequestration of carbon (Falkowski, Barber,  
 37      & Smetacek, 1998) on timescales ranging from days to years depending on the sink-  
 38      ing depth and circulation. Understanding the mechanisms driving the export of POC  
 39      from the ocean's surface to the interior is therefore crucial to better constrain Earth's  
 40      carbon budget.

41      Traditionally, POC export is thought to occur through gravitational sinking and  
 42      one-dimensional models have been used to describe the sinking POC flux with depth.  
 43      Particles produced through primary and secondary production in the surface layer  
 44      that are relatively large and fast-sinking, tend to sink out of the upper surface layer  
 45      on timescales shorter than the timescale on which the particles get remineralized.  
 46      It is reasonable to treat POC export as sinking-dominated if the vertical advective  
 47      velocities in the ocean are weaker than the velocities associated with gravitational  
 48      sinking. However, Particulate Organic Matter (POM) has a wide range of particle  
 49      shape, size and type, that result in particle sinking velocities ranging from practically  
 50      zero, to several hundreds of meters per day. The size spectrum, or number distribution  
 51      of particle sizes, is usually characterized by a power law with the power ranging between  
 52      -2 and -4, for which the abundance of small particles is  $\mathcal{O}(10^4 - 10^8)$  greater than large  
 53      particles. The biomass size spectrum, which indicates the distribution of biomass vs.  
 54      particle size, tends to be flatter and variable in shape (Sheldon, Prakash, & Sutcliffe,  
 55      1972) compared to the particle number spectrum, because the volume (and mass) of  
 56      a particle scales with its linear size raised to a power that exceeds 1 (and typically  
 57      varies between 2 and 3 depending on shape and porosity). Importantly, it means that a  
 58      significant fraction of the particulate biomass is in the small size fraction. Even though  
 59      the sinking velocity  $w_s$  of particles does not perfectly relate to particle size  $l$ , it is fair to  
 60      assume that  $w_s \sim l^n$  (with  $n = 2$  according to Stokes law, and  $1 < n < 2$  for complex  
 61      particle shapes). Due to this, as well as the fact that particles of organic matter are  
 62      not very much greater in their densities than seawater, a significant fraction of the

63 biomass sinks very slowly (at velocities less than tens of meters per day). When the  
 64 gravitational sinking velocity of particles is comparable to (or smaller than) the vertical  
 65 velocities in the flow field, the dynamics of the flow field can impact the trajectories  
 66 and fate of the POC. Thus, depending on the flow dynamics, and the fraction of slow-  
 67 sinking particulate biomass, the sinking of organic matter can be affected by the fluid  
 68 flow in the ocean.

69 Recent studies have shown that ocean dynamics can play a role in driving the  
 70 transport of carbon from the euphotic layer to the ocean interior. For example, en-  
 71 hanced vertical velocities along the edge of a mesoscale eddy led to a funneling of par-  
 72 ticles along the eddy's periphery (van Haren, Millot, & Taupier-Letage, 2006; Waite  
 73 et al., 2016). Omand et al. (2015) found that submesoscale mixed layer eddies, while  
 74 contributing to the restratification of a frontal zone, were subducting a large amount  
 75 of non-sinking POC from the surface productive layer during the onset of the Spring  
 76 bloom in the subpolar North Atlantic. Advectively subducting plumes or filaments  
 77 of high oxygen, chlorophyll and small POC (evidenced through backscatter) were de-  
 78 tected from a suite of gliders during the North Atlantic Bloom experiment (Alkire et  
 79 al., 2012). Using model simulations to capture the process of eddy-driven subduction,  
 80 Omand et al. (2015) estimated the downward advective flux of non-sinking POC and  
 81 parameterized it. Briggs et al. (2011) quantified the flux of fast-sinking particles con-  
 82 sisting largely of diatoms from observations of optical backscatter. But, these estimates  
 83 did not account for a range of sinking particle velocities. Typically, particulate organic  
 84 matter (POM) has a wide spectrum of sinking velocities and in order to understand  
 85 its fate and export, we need to consider the biomass distribution as a function of the  
 86 particle sinking velocity spectrum and its interaction with the dynamics of the flow  
 87 field in the ocean.

88 A growing body of literature focusing on submesoscale (1-10 km) dynamics is  
 89 exploring its impact on biogeochemical processes (Lévy, Ferrari, Franks, Martin, &  
 90 Rivière, 2012; Mahadevan, 2016). Submesoscale dynamics, characterized by Rossby  
 91 numbers of order 1, typically develop in filaments in areas where sharp density fronts  
 92 exist (Klein & Lapeyre, 2009; McWilliams, 2016; Thomas, Taylor, Ferrari, & Joyce,  
 93 2013). In this dynamical regime, geostrophic balance breaks down and a secondary  
 94 ageostrophic circulation develops across the front, capable of generating large vertical  
 95 velocities on the order of 100 m/day (Fox-Kemper, Ferrari, & Hallberg, 2008; Mahade-  
 96 van, 2016). On the denser side of the front, the vorticity is cyclonic and associated with  
 97 downwelling velocities, while anticyclonic vorticity and upwelling is expected on the  
 98 lighter side of the front. The distribution of relative vorticity across a front is asym-  
 99 metric and skewed toward cyclonic vorticity (Rudnick, 2001), leading to more localized  
 100 and more intense downwelling regions, as opposed to weaker and larger upwelling re-  
 101 gions (Mahadevan & Tandon, 2006). Enhanced vertical velocities can generate a local  
 102 bloom by supplying nutrients to the sunlit layer of the ocean (Lévy, Klein, & Treguier,  
 103 2001; Mahadevan & Archer, 2000), or can significantly increase the export of POC to  
 104 the ocean interior through downwelling (Estapa et al., 2015; Gruber et al., 2011; Lévy  
 105 et al., 2012; Omand et al., 2015).

106 The downwelling velocities  $\mathcal{O}(100 \text{ m/day})$  generated at submeso-scales provide  
 107 a physical mechanism capable of competing with gravitational sinking and thus ex-  
 108 porting particles over a larger portion of the particle size spectrum. Through this  
 109 mechanism, smaller particles can be exported on timescales shorter than their rem-  
 110 ineralization timescales, despite their slower sinking velocities. Depending on the frac-  
 111 tion of biomass in smaller particles (i.e., with slow sinking velocities), the impact of  
 112 submesoscale dynamics on the export of POC is potentially significant.

113 In this study, we account for a range of particle sinking velocities in a dynamic  
 114 flow field. Despite progress on sampling and viewing particles in the ocean (McDonnell  
 115 & Buesseler, 2010), direct measurements of particles sinking velocities are difficult

116 to obtain, and often inferred from key parameters such as particle type, size, and  
 117 density. Though we acknowledge a large variability in these relationships, we assume  
 118 a relationship between particle size, biomass, and particle sinking velocity in order to  
 119 assess the impact of the flow dynamics and particle size spectrum on the export flux.

120 We rely on a submesoscale-resolving, non-hydrostatic ocean model to simulate the  
 121 dynamics in the upper few hundred meters of the ocean. The model does not represent  
 122 surface waves or boundary layer turbulence, but rather, examines the fate of particulate  
 123 organic matter beneath the turbulent surface boundary layer. The dynamical model  
 124 is coupled with a particle-tracking module to model the advection of particles by fluid  
 125 flow, while neglecting the effects of particle inertia and drag on their advection. In  
 126 addition, the particles sink with a range of sinking velocities (between 0.025–5 m  
 127 day<sup>-1</sup>).

128 The model is used to quantify the contribution of slow-sinking particles to carbon  
 129 export, as a function of (1) the dynamics of the flow field, (2) the slope of the sinking  
 130 velocity spectrum, and (3) the remineralization timescale. Particles in the model  
 131 are prescribed with both a constant and time-varying sinking velocity to mimic a  
 132 remineralizing behavior. Particles are released in two fundamentally different flow  
 133 fields in terms of dynamics based on observed conditions in the Northeast Pacific:  
 134 In the summer, where ocean dynamics are characterized by low Rossby numbers and  
 135 weak vertical advective velocities, and in the winter, where ocean dynamics include  
 136 submesoscale frontal structures and local Rossby numbers  $\mathcal{O}(1)$ . Both simulations  
 137 and the particle-tracking module are described in Section 2. The impact of particles  
 138 characteristics and ocean dynamics on the export of POC is quantified in Section 3,  
 139 and discussed in Section 4. Section 5 summarizes the key conclusions of the study.

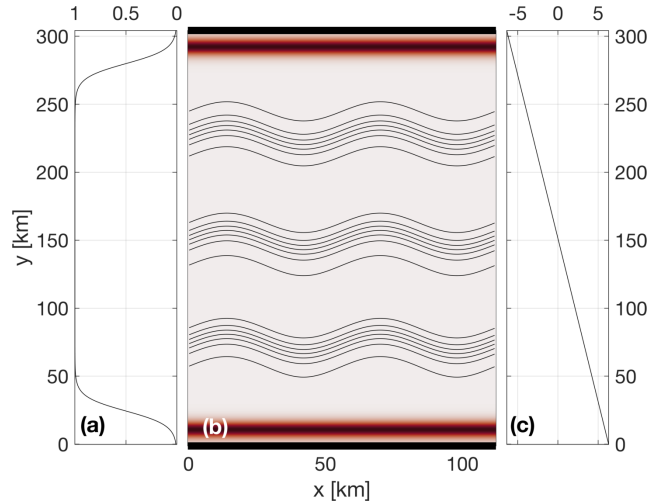
## 140 2 Methods

### 141 2.1 Model setup and domain

142 This study uses a non-hydrostatic, three-dimensional, Process Study Ocean Model  
 143 (PSOM; Mahadevan, Olinger, & Street, 1996a, 1996b) to simulate an eddy field that is  
 144 representative of the Northeast Pacific Ocean. The model is set in a channel configura-  
 145 tion with periodic east-west boundaries, and solid boundaries in the south and north.  
 146 The domain covers 112 km in the x-direction, 304 km in the y-direction, and 1000 m  
 147 in the vertical (Figure 1). The horizontal resolution is 500 m, while a stretched grid is  
 148 used in the vertical with 32 levels ranging in thickness from 1.25 m near the surface to  
 149 70 m at the lowermost level. The model is integrated numerically in time and evolves  
 150 the temperature, salinity, free-surface height, pressure, and three-dimensional velocity  
 151 field from an initial state, subject to momentum and buoyancy fluxes applied through  
 152 the surface boundary.

160 Time-varying wind stress and heat flux are prescribed at the surface boundary.  
 161 Time series are computed from measurements collected at Station Papa and available  
 162 through the Pacific Marine Environmental Laboratory (Laboratory, 2018). Daily wind  
 163 stress and net heat fluxes are calculated over the period 2007–2016 to produce a year-  
 164 long climatology. A squared low-pass filter with a cut-off frequency of 8.5 days is  
 165 applied to both time series to remove high-frequency variability. In all numerical  
 166 experiments, simulations are run for the first 5 days without any forcing applied to  
 167 the surface boundary. Surface wind stress and heat fluxes are then linearly ramped up  
 168 between days 5 and 10 of the simulation, to reach realistic values at day 10.

169 While the meridional component,  $\tau_y$ , is set to zero, the zonal component of  
 170 the wind stress,  $\tau_x$ , is prescribed at the surface throughout the model domain and  
 171 is tapered at the northern and southern boundaries to avoid excessive Ekman-driven  
 172 upwelling and downwelling (Figure 1a). A restoration timescale is prescribed to contain



153 **Figure 1.** PSOM model setup. (a) Meridional profile of scaling coefficient that multiplies the  
 154 time-varying zonal wind stress  $\tau_x$  shown in Fig. 3a. The taper at north and south boundaries  
 155 prevents ‘coastal’ up-/down-welling being entirely concentrated in the boundary grid cell. (b)  
 156 Restoration factor (color shading) used to dampen internal wave reflection at boundaries as well  
 157 as up-/down-welling due to the windstress curl. Surface density contours (black) show the three  
 158 fronts used to initialize the model. (c) Meridional variation of the time-dependent surface heat  
 159 flux (Fig. 3a) prescribed over the domain.

173 the curl-driven upwelling and downwelling regions generated by the tapering of the  
 174 wind stress, as well as to limit internal wave reflection at the solid boundaries back  
 175 into the domain (Figure 1b). While net surface heat fluxes are homogeneous in the  
 176 zonal direction, a meridional gradient is maintained throughout the simulation. The  
 177 meridional gradient was determined from the North American Regional Reanalysis  
 178 (NARR) product (Mesinger et al., 2006), and set to  $1/24 \text{ W/m}^2/\text{km}$  (Figure 1c).

179 Initial hydrographic conditions are determined from a three-dimensional gridded  
 180 field of temperature and salinity from Argo floats (Gaillard, 2015; Gaillard, Reynaud,  
 181 Thierry, Kolodziejczyk, & von Schuckmann, 2016). Argo data is averaged monthly  
 182 over the period 2002–2012 and two different months are used to initialize the two main  
 183 numerical experiments for this study: Climatological conditions in April are used to  
 184 initialize the *Papa\_summer* experiment, while January climatological conditions are  
 185 used to initialize the *Papa\_winter* experiment (Table 1). The north-south background  
 186 density gradient is then intensified into three fronts located at  $y = 75$ ,  $y = 150$ , and  
 187  $y = 225 \text{ km}$  (Figure 1). The amplitude of the density gradient associated with the three  
 188 fronts is determined from the probability distribution function (PDF) of the density  
 189 gradients measured by underwater gliders deployed around Station Papa over the  
 190 period 2008–2010 (Pelland, 2018; Pelland, Eriksen, & Cronin, 2016). To reduce model  
 191 spin-up time, density fronts are perturbed by a sinusoidal wave with a wavelength close  
 192 to the 1st baroclinic deformation radius ( $\lambda = 66 \text{ km}$ ). Similar PSOM configurations  
 193 were successfully used in previous studies (Mahadevan, D’Asaro, Lee, & Perry, 2012;  
 194 Omand et al., 2015).

195 Two main experiments are conducted using the same configuration of PSOM,  
 196 where only initial conditions and surface forcings are varied: *Papa\_summer* aims  
 197 at generating ocean dynamics representing conditions in the Northeast Pacific in  
 198 the summertime. Summer ocean dynamics are characterized by a flow generally in

220 **Table 1.** Summary of the key characteristics of PSOM experiments *Papa-summer* and  
 221 *Papa-winter*.

	<i>Papa-summer</i>	<i>Papa-winter</i>
Time period	April – July	January – March
Spin-up	60 days	50 days
Advective timestep	216 s	108 s
Horizontal diffusivity	1 m <sup>2</sup> s <sup>-1</sup>	0.2 m <sup>2</sup> s <sup>-1</sup>
Restoration timescale	3 days	15 days
Zonal wind stress	0 – +0.16 N m <sup>-2</sup>	-0.05 – +0.17 N m <sup>-2</sup>
Surface heat flux	-46.8 – +167.5 W m <sup>-2</sup>	-57.6 – +15.3 W m <sup>-2</sup>
Maximum M <sup>2</sup> ( $\times 10^{-8}$ )		
initial	3.2 s <sup>-2</sup>	33.9 s <sup>-2</sup>
spun-up	12.0 s <sup>-2</sup>	50.0 s <sup>-2</sup>
Maximum N <sup>2</sup> ( $\times 10^{-4}$ )		
initial	1.5 s <sup>-2</sup>	1.6 s <sup>-2</sup>
spun-up	3.1 s <sup>-2</sup>	1.1 s <sup>-2</sup>
Averaged mixed layer depth		
initial	73 m	85 m
spun-up	11 m	93 m

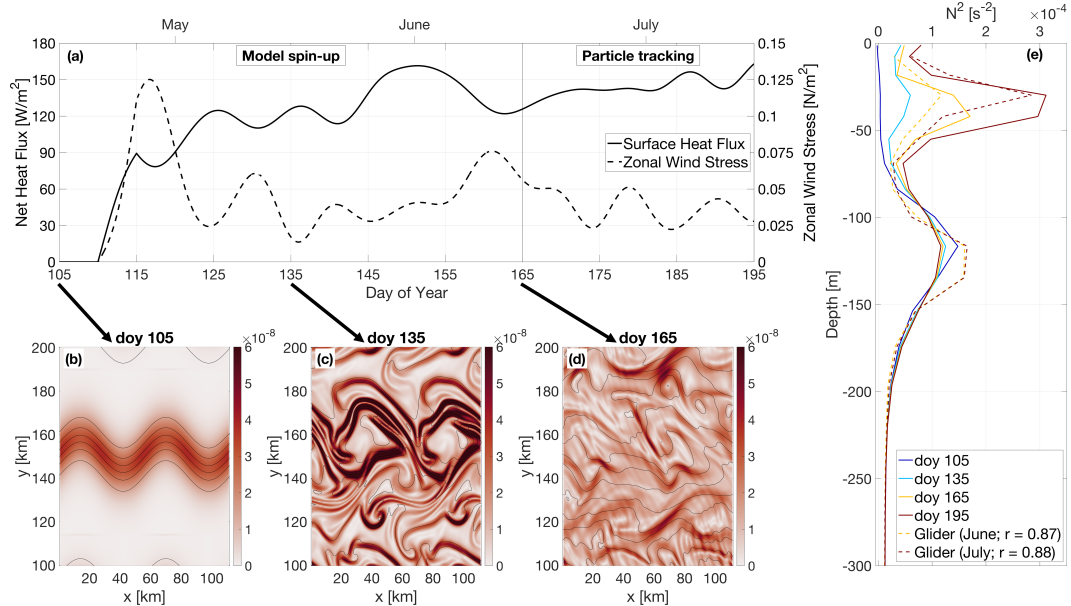
199 geostrophic balance, with relatively weak density gradients and low Rossby numbers  
 200 ( $\ll 1$ ). *Papa-winter* aims at capturing wintertime ocean conditions in the region. A  
 201 different dynamical regime is expected to dominate during wintertime when mixed  
 202 layers are deeper and lateral density gradients enhanced, with sharper density fronts,  
 203 filament-like features and localized Rossby number  $\mathcal{O}(1)$  over spatial scales  $\mathcal{O}(1 \text{ km})$   
 204 (Callies, Ferrari, Klymak, & Gula, 2015; Mensa et al., 2013; Thompson et al., 2016).  
 205 The individual characteristics of each of  
 206 *Papa-summer* and *Papa-winter* are detailed below.

### 207 2.1.1 *Papa-summer* Model Experiment

208 In *Papa-summer*, PSOM is initialized based on climatological Argo data in April.  
 209 The magnitude of the density gradient across the front is set to  $3.34 \times 10^{-6} \text{ kg/m}^3/\text{m}$ ,  
 210 which corresponds to the 95<sup>th</sup> percentile of the PDF of density gradients measured  
 211 in April from glider data collected in the region (Figure 2 and Table 1). The model  
 212 is run with a timestep of 216 s and is allowed to spin-up for 60 days, allowing sum-  
 213 mer stratification to develop. The model is then run for 30 additional days, saving  
 214 instantaneous model fields every 3 hours for particle tracking. The month of April  
 215 is chosen for initialization so the experiment would capture the onset of positive net  
 216 heat fluxes, and the summer restratification that ensues in July-August (Figure 2). In  
 217 this region, the summer stratification is associated with large primary productivity,  
 218 particle production, and POC export (e.g., fecal pellets, dead phytoplankton; Plant  
 219 et al., 2016).

### 231 2.1.2 *Papa-winter* Model Experiment

232 In *Papa-winter*, PSOM is initialized based on climatological Argo data in January.  
 233 The frontal gradient is set to  $3.54 \times 10^{-5} \text{ kg/m}^3/\text{m}$ , which corresponds to the  
 234 99<sup>th</sup> percentile of the PDF of density gradients measured in January from glider data  
 235 collected in the region (Figure 3 and Table 1). The model is allowed to spin-up for 50  
 236 days allowing for the prescribed fronts to become unstable. To accommodate for the

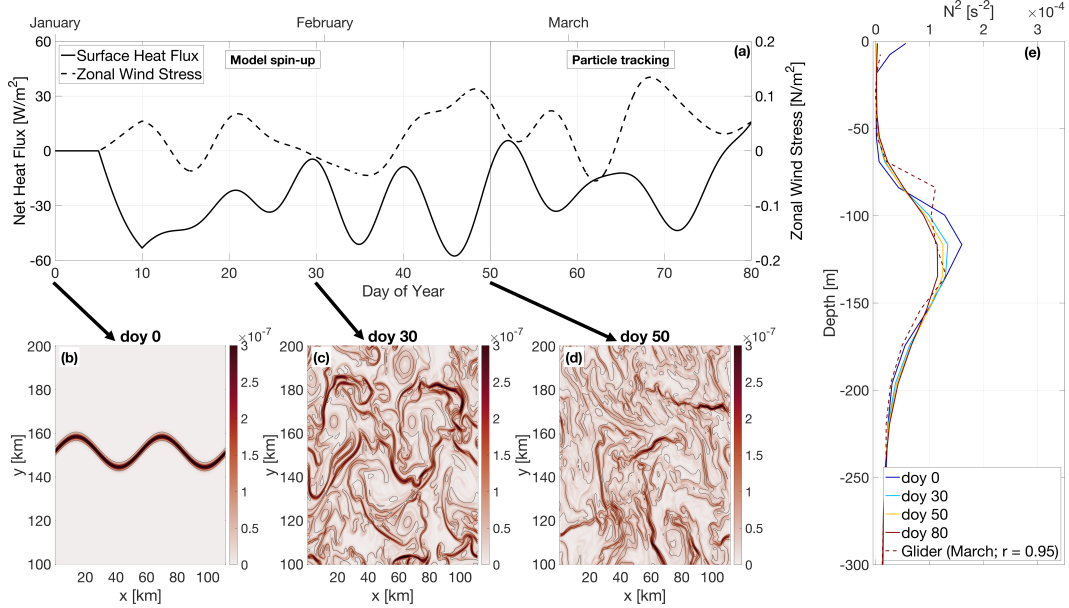


222 **Figure 2.** PSOM configuration for *Papa\_summer*. (a) Time series of net heat fluxes and wind  
 223 stress prescribed at the surface. Notice the positive heat fluxes, as well as downfront winds (i.e.  
 224 eastward) persisting throughout the experiment. (b)-(d) surface horizontal buoyancy gradients  
 225  $M^2 = |\nabla_H b|^2$  (in  $s^{-2}$ ) at day of year (doy) 105, 135, and 165. Black contours show isopycnals (in  
 226 kg/m<sup>3</sup>; CI = 0.01 kg/m<sup>3</sup>). (e) Vertical profile of the buoyancy frequency  $N^2$  at day of year 105,  
 227 135, 165, and 195, showing the development of summer stratification centered at  $z = 30$  m (solid  
 228 lines). Monthly-average vertical stratification obtained from glider profiles collected in June and  
 229 July are superimposed (dashed lines), along with the correlation coefficient between observations  
 230 and model outputs.

237 larger density gradients and stronger velocities, the advective timestep is shortened to  
 238 108 s and the horizontal diffusivity is lowered to 0.2 m<sup>2</sup>/s throughout the experiment.  
 239 The model is run for 30 additional days, saving instantaneous model fields every 1.5  
 240 hours for particle tracking. The month of January is chosen for initialization so the  
 241 experiment would capture the time of year where the mixed layer is the deepest, and  
 242 Rossby number  $O(1)$  occur more frequently. The objective is for this experiment to  
 243 contrast *Papa\_summer* by capturing the statistics of ocean conditions dominated by  
 244 submesoscale dynamics.

### 253 2.1.3 Validation

254 To ensure that PSOM simulations yielded realistic conditions for both *Papa\_summer*  
 255 and *Papa\_winter*, distributions of horizontal ( $M^2$ ) and vertical ( $N^2$ ) buoyancy gradi-  
 256 ents are compared with glider observations collected over the period 2008-2009 (Pelland  
 257 et al., 2016). During this period, underwater gliders sampled in a “bow-tie” pattern  
 258 centered on Station Papa. Gliders sample the water column in a triangular wave  
 259 pattern, whose shape is easily affected by currents, due to the slow moving speed of  
 260 the glider (~1 km/hr). It is therefore challenging to associate a specific spatial scale  
 261 with gradients computed between glider profiles, as profile separation distances can be  
 262 highly variable through depth and time. To circumvent this issue, horizontal buoy-  
 263 ency gradients are computed between each pair of glider profiles available within one  
 264 branch of the bow-tie. Each along-track lateral buoyancy gradient is thus associated



245 **Figure 3.** PSOM configuration for *Papa\_winter*. (a) time series of net heat fluxes and wind  
 246 stress prescribed at the surface. Notice the mostly negative heat fluxes, as well as alternating  
 247 zonal wind direction. (b)-(d) surface horizontal buoyancy gradients  $M^2 = |\nabla_H b|^2$  (in  $s^{-2}$ ) at day  
 248 of year (doy) 0, 30, and 50. Black contours show isopycnals (in  $kg/m^3$ ; CI =  $0.01\ kg/m^3$ ). (e)  
 249 Vertical profile of the buoyancy frequency  $N^2$  at doy 0, 30, 50, and 80, showing the persistence  
 250 of the halocline between  $z = 80$  and  $z = 180$  m throughout the experiment (solid lines). Monthly-  
 251 average vertical stratification obtained from glider profiles collected in March is superimposed  
 252 (dashed line), along with the correlation coefficient between observations and model outputs.

265 with a specific separation scale and a timestamp. Glider-based density gradients can  
 266 be affected by internal waves. To filter the impact of internal waves on the PDF of  
 267 horizontal buoyancy gradients, only gradients computed at a scale of twice the Rossby  
 268 radius  $\pm 1$  km are considered. Rossby radii are estimated from the glider data and  
 269 are  $\sim 8$  km in winter and  $\sim 20$  km in summer.

## 270 2.2 Particle Tracking Experiments

### 271 2.2.1 Particle Advection Scheme

To quantify the impact of submesoscale dynamics on the export of Particulate Organic Matter (POC), Lagrangian particle trajectories are computed using the same scheme as in “TRACMASS” (Döös, Kjellsson, & Jönsson, 2013) with the flow fields from the two experiments described above. The three-dimensional, non-divergent velocity components from the faces of each “C” grid cell are linearly interpolated onto the particle’s position within the grid cell. For example, the eastward (along the x-axis) velocity of a particle is given by

$$u(x) = u_{i-1} + \frac{(x - x_{i-1})}{(x_i - x_{i-1})}(u_i - u_{i-1}), \quad (1)$$

where the subscripts  $i - 1$  and  $i$  denote the western and eastern walls of the grid cell where the particle is located, respectively. This can be re-written as

$$\frac{\partial x}{\partial t} + \beta x + \delta = 0, \quad (2)$$

where  $\beta = (u_i - u_{i-1})/\Delta x$  and  $\delta = -u_{i-1} - \beta x_{i-1}$  (Döös et al., 2013). This differential equation can be solved analytically for  $\beta \neq 0$  as

$$x_{t_1} = \left( x_0 + \frac{\delta}{\beta} \right) \exp^{-\beta(t_1-t_0)} - \frac{\delta}{\beta} \quad (3)$$

The time it will take for the particle to reach the eastern or western face of the grid cell can be computed by taking  $x_{t_1} = x_i$  or  $x_{t_1} = x_{i-1}$ , respectively, and solving for  $t_1$ . For each advective timestep, the times required for the particle to reach any of the 6 walls of the grid cell are computed using (3). If any of those times is shorter than the advective timestep, the particle is advected until it reaches the cell wall. Then the flow field in the adjacent grid cell is considered and the particle is advected over the remaining time.

### 2.2.2 Particle Seeding

For all particle-tracking experiments, a single particle seeding event is prescribed. In the horizontal, particles are seeded every 250 m over the entire domain in the x-direction, and for  $100 < y < 200$  km in the y-direction. The seeding is centered over the mean position of the central front (see Figure 2) and is therefore not affected by undesired effects created by the solid north-south solid boundaries. In the vertical, particles are seeded every 1 m between 75 and 85 m. This depth range is chosen as it corresponds to the average euphotic depth at Station Papa, defined by the 1% light level. The euphotic depth was computed for the months of February and June over the period 2007-2016 from profiles of Photosynthetically Available Radiation (PAR) collected at Station Papa as part of the long-term monitoring of Line P executed by the Department of Fisheries and Ocean Canada<sup>1</sup>. The average euphotic depth computed for both of these months is around 80 m, which agrees with previously established estimates of the euphotic depth (Harrison, Whitney, Tsuda, Saito, & Tadokoro, 2004; Sherry, Boyd, Sugimoto, & Harrison, 1999).

In each particle-tracking experiment, four different classes of particles are released. Each particle class is characterized by a different sinking velocity: 0.025, 0.05, 1, and 5 m/day. The slowest-sinking class is essentially selected to represent non-sinking particles: based on the setup of our experiments, the slowest-sinking particles would take 800 days on average to be exported to a depth of 100 m through gravitational sinking, a timescale much greater than commonly observed remineralization timescales. The fastest-sinking velocity is chosen as an end-member velocity class of particle that will be exported in its entirety over the course of our experiment.

The advective timestep for particles is set to 1.5 hours. The flow field is linearly interpolated in time between model outputs, justifying the higher temporal resolution used for particle tracking in *Papa\_winter*. Particle positions are saved every 3 hours, along with key model variables interpolated onto the particle positions (e.g., density, vorticity). Particles are tracked for three weeks (28 days). Each particle-tracking experiment contains 1,971,717 particles per sinking-velocity class, for a total of 9,858,585 particles. Particles located deeper than the maximum winter mixed layer (i.e., 100 m; Pelland et al., 2016; Plant et al., 2016) are considered exported, as they will likely not be re-entrained into the mixed layer.

### 2.2.3 Density and Biomass Spectra

The slope  $\xi$  of the size spectrum of particles (also known as the Junge slope; White et al., 2015) is the slope of the log-log curve of particle number  $N$  vs. particle radius

<sup>1</sup> <https://www.waterproperties.ca/linep/index.php>

*r*, where

$$N(r) = N_0 \left( \frac{r}{r_0} \right)^{-\xi}. \quad (4)$$

Here,  $N_0$  and  $r_0$  represent a reference particle number and radius, chosen arbitrarily. For small particles ( $<400 \mu\text{m}$ ) and relatively low temperature ( $<15^\circ\text{C}$ ), it has been shown that the relationship between particle radius  $r$  and sinking velocity  $w_s$  exhibits a range of variation and is difficult to determine empirically. Nevertheless, Stokes' law, where  $w_s \propto r^2$ , is often used as a lower-bound sinking velocity estimate (Bach et al., 2012).

Assuming a Stokes-like relationship, we can construct a particle sinking velocity spectrum  $N(w_s)$  based on (4), as

$$N(w_s) = N_0 \left( \frac{w_s}{w_{s0}} \right)^{-\xi/2}, \quad (5)$$

where  $w_{s0}$  is the sinking speed of particles with radius  $r_0$ . For a specific slope and sinking-velocity class, an equivalent number of particles per simulated particle can be computed using (5) (See Figure 4). For example, using the largest sinking velocity class as a reference (i.e.,  $w_{s0} = 5 \text{ m/day}$  and  $N_0 = 1,971,717$ ), and a spectral slope  $\xi = 4$ , each simulated particle with a sinking velocity of  $0.025 \text{ m/day}$  in fact represents 40,000 particles (Figure 4). The relative biomass of a particle in a specific sinking-velocity class,  $B_p(w_s)$  can be estimated if the biomass is assumed to scale with the particle's volume. The relative biomass of one particle in a sinking-velocity class  $w_s$  can therefore be computed as

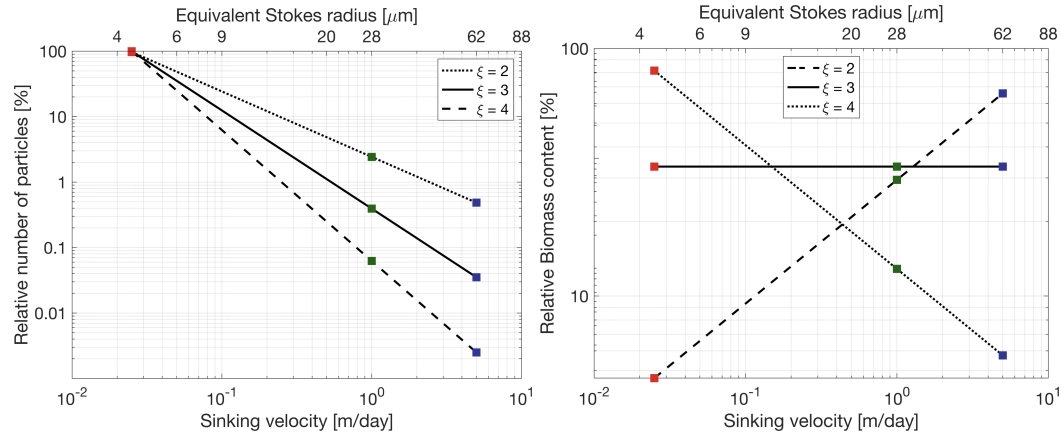


**Figure 4.** Relative number of particles (left) and biomass (right) as a function of sinking velocity  $w_s$ . Sinking velocity spectrum are shown for three different Junge slope  $\xi$ : 2 (dotted), 3 (solid), and 2 (dashed). Colored squares indicate the sinking velocities of the three particle classes modeled:  $0.025 \text{ m/day}$  (red),  $1 \text{ m/day}$  (green), and  $5 \text{ m/day}$  (blue).

$$B_p(w_s) = B_p(w_{s0}) \left( \frac{w_s}{w_{s0}} \right)^{3/2} \quad (6)$$

where  $B_p(w_{s0})$  is the biomass of a particle in the sinking velocity class  $w_{s0}$ . The total biomass associated with one simulated particle can be obtained by scaling (6) by the ratio  $N(w_s)/N_0$ :

$$B(w_s) = B_0 \left( \frac{w_s}{w_{s0}} \right)^{3/2} \frac{N(w_s)}{N_0} \quad (7)$$

where  $B_0 = B_p(w_{s_0})$ . Combining (5) and (7) yields an expression relating the biomass associated with a simulated particle for a specific sinking-velocity class and the spectral slope (Figure 4):

$$B(w_s) = B_0 \left( \frac{w_s}{w_{s_0}} \right)^{\frac{3-\xi}{2}}. \quad (8)$$

Using the same example as before where  $\xi = 4$ , if the amount of biomass associated with one simulated particle in the 5 m/day sinking-velocity class is taken as  $B_0 = 1$ , then one simulated particle sinking at 0.025 m/day contains 14.14 units of biomass and a single particle contains  $14.14/40,000 = 3.5 \times 10^{-4}$  units of biomass (see Figure 4). This normalized formulation of particle number and biomass (see Equations (5) and (8)) has the advantage that the impact of spectral slope on the relative export of biomass can be quantified without needing a large number of particle-tracking experiments, where the number of seeded particles would vary to account for the different spectral slopes. For the purpose of this study, only the relative amount of biomass is relevant. For simplicity, we define a normalized biomass unit for  $\xi = 3$  as  $B_0 = 1$ . The values taken by  $B_0$  for other Junge slopes  $\xi$  are computed under the condition that the total amount of biomass is kept constant (Figure 4b).

#### 2.2.4 Particle Remineralization Scheme

Remineralization of particles as they sink through the water column impacts the amount of biomass exported. Slow-sinking particles generally contain less biomass and spend more time in the mixed layer, which means that they are remineralized at a shallower depth than faster sinking particles. Remineralization processes are complex, species-dependent, and generally not well-understood. In the absence of a consensus on a general functional form of particle remineralization, we rely on an idealized relationship which assumes that the biomass content of a particle decreases in time proportionally to the particle volume. Remineralization is thus modeled as an exponential decrease of biomass with time at a rate  $k$  (Iversen & Ploug, 2010, 2013)

$$B(t) = B^0 \exp(-kt), \quad (9)$$

where  $B^0$  denotes the biomass content at  $t = 0$  days, and the remineralization rate is taken to be  $k = 0.13 \text{ day}^{-1}$  in this study (Iversen & Ploug, 2010). This remineralization rate is independent of particle sinking velocity, and seems to lie within the range of other estimates (Iversen & Ploug, 2010, 2013; Ploug, Iversen, Koski, & Buitenhuis, 2008). The change in biomass with time is in turn expected to affect the sinking velocity of the particle. Given that  $B \propto w^{3/2}$  (see Equation (6)), particles in all sinking-velocity classes undergo a decay in sinking speed according to

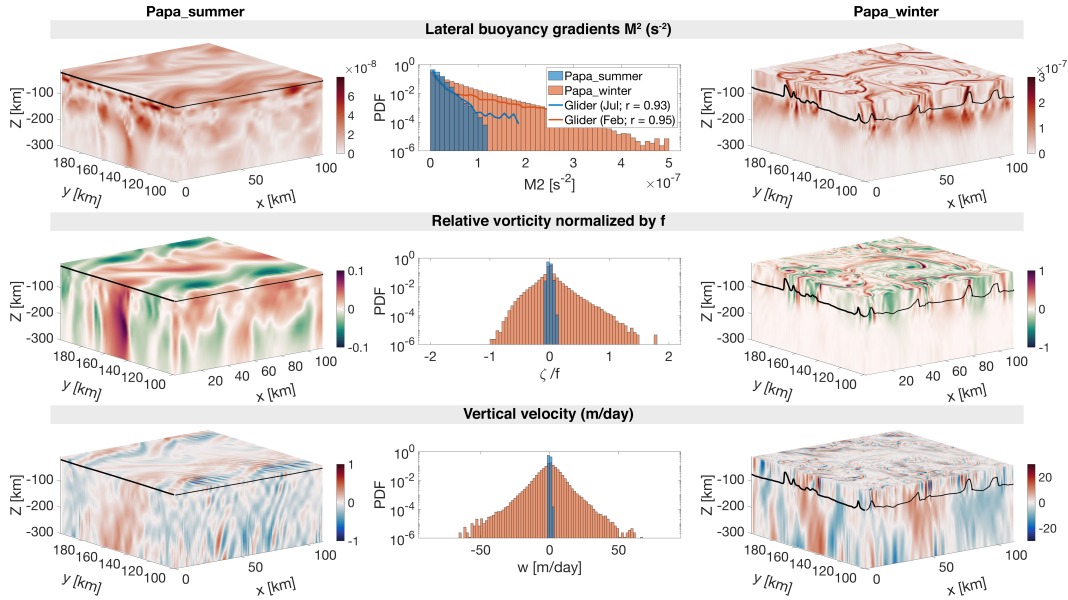
$$w_s(t) = w_s^0 \exp\left(-\frac{2kt}{3}\right), \quad (10)$$

where  $w_s^0$  is the initial sinking velocity at  $t = 0$  days. In this study, the impact of remineralization is thus considered through the implementation of a time-dependent sinking velocity (Equation 10). While particles classes are classified based on their initial sinking-velocity, it is worth noting that over the length of the particle-tracking experiments that include remineralization (28 days), particle sinking speeds slow down to 10% of their initial velocity.

### 3 Results

#### 3.1 Seasonally varying dynamical regimes

Two model experiments are designed to capture different dynamical conditions observed in the Northeast Pacific Ocean in summer and winter. *Papa\_summer* is initialized in early spring (doy 105) when the water column is characterized by a relatively



365 **Figure 5.** Snapshots of  $M^2$  (top),  $\zeta/f$  (middle), and  $w$  (bottom) half-way through the  
 366 particle tracking experiment for *Papa\_summer* (left) and *Papa\_winter* (right), with the Mixed  
 367 Layer Depth indicated by the solid black line. The corresponding Probability Distribution  
 368 Functions (PDFs) are shown in the center for both *Papa\_summer* (blue) and *Papa\_winter* (red). Note the  
 369 different colorbars used for *Papa\_summer* and *Papa\_winter*. Histograms of  $M^2$  computed from  
 370 glider data at Station Papa in February (blue line) and July (red line) are superimposed in the  
 371 top middle panel.

346 deep mixed layer ( $\sim 100$  m) and a halocline located between 100 and 150 m (Figure  
 347 2). The forcing by a realistic, positive, net heat flux generates the restratification of  
 348 the water column, with the development of a strong thermocline between 25 and 50 m  
 349 leading to the shoaling of the mixed layer and a subsurface peak in  $N^2$  at about 30 m  
 350 (see Figure 2). A comparison between model outputs and monthly-averaged density  
 351 profiles from underwater gliders collected in June and July over the period 2008-2009  
 352 yields correlation coefficients of  $r = 0.87$  and  $r = 0.88$ , respectively. These high cor-  
 353 relation suggest that *Papa\_summer* numerical experiment captures the vertical spring  
 354 and summer conditions in the Northeast Pacific Ocean.

355 In the horizontal, the prescribed density fronts progressively become unstable  
 356 within the first 60 days of the experiment (Figure 2). During this time, the Total  
 357 Kinetic Energy ( $KE_{tot}$ ) contained in the model domain slowly increases before reach-  
 358 ing a maximum at day 162, where it remains relatively constant for the rest of the  
 359 simulation. The flattening of the  $KE_{tot}$  curve is used to determine the time necessary  
 360 for the simulation to spin-up, hence determining the start day of the particle-tracking  
 361 experiments. The ocean dynamics associated with *Papa\_summer* are characterized  
 362 using PDFs of horizontal buoyancy gradients ( $M^2 = |\nabla_H b|^2$ ), vertical velocities ( $w$ ),  
 363 and Rossby numbers computed from the normalized vertical component of the relative  
 364 vorticity ( $Ro = (v_x - u_y)/f$  where  $f = 1.12 \times 10^{-4}$ ; Figure 5).

372 Lateral buoyancy gradients in the summer are relatively weak  $\mathcal{O}(10^{-8} \text{ s}^{-2})$  and  
 373 result in low Rossby numbers  $\mathcal{O}(0.1)$ , with positive relative vorticity on the denser  
 374 (north) side of the front and negative relative vorticity on the lighter (south) side  
 375 of the front. Corresponding vertical velocities are consistently weaker than 1 m/day

( $<10^{-5}$  m/s) and are characterized by regions of weak upwelling and downwelling on 10 km scales, associated with the meandering of the front (Bower & Rossby, 1989). Alternating bands of upwelling and downwelling at  $\mathcal{O}(1 \text{ km})$  spatial scale are superimposed, and likely caused by propagating internal waves. Coherent vertical velocity structures extend to depths much greater than the mixed layer depth ( $\sim 25 \text{ m}$ ; Figure 5). The amplitude of the vertical velocity field coincides with the expected order of magnitude given by the scaling  $w \propto RofU/N$  (Mahadevan, 2016): using  $Ro \sim 0.1$  (Figure 5),  $N \sim 10^{-2} \text{ s}^{-1}$  (Figure 2),  $f \sim 10^{-5} \text{ s}^{-1}$ , and  $U \sim 0.01 \text{ m/s}$ , we obtain  $w \sim 10^{-6} \text{ m/s}$ , or  $\sim 10^{-1} \text{ m/day}$ .

*Papa-winter* is, on the other hand, initialized in the winter (doy 0) to capture a time period where the mixed layer depth is deeper ( $\sim 100 \text{ m}$ ) and density gradients more pronounced (Pelland et al., 2016). At this time of year, the water column in this region is characterized by the presence of a deep halocline between 100 and 150 m (Figure 3 Pelland et al., 2016). After spin-up, the vertical stratification remains consistent throughout the model run, and compares well with the vertical profile obtained from glider observations for the month of March ( $r = 0.95$ ; see Figure 3). In the horizontal, prescribed density fronts are much sharper than in summer (i.e., over smaller spatial scales  $\mathcal{O}(1 \text{ km})$  vs.  $\mathcal{O}(10 \text{ km})$ ). Because of these stronger density gradients, combined with the alternating zonal winds and constantly negative surface heat flux, the fronts become unstable more rapidly than in summer (Figure 3). As a result,  $KE_{\text{tot}}$  starts to plateau at doy 48. The experiment is considered spun-up by doy 50 and the particle-tracking experiment is initialized.

The frontal structures visible in the horizontal buoyancy gradient field are associated with filaments of relatively high Rossby number of  $\mathcal{O}(1)$  (Figure 5). The PDF of relative vorticity reveals a positively-skewed distribution ( $s = 0.68$ ). This is in agreement with the fact that the relative vorticity is more likely to be cyclonic than anticyclonic, based on conservation of potential vorticity (Hoskins & Bretherton, 1972). Regions with high Rossby number are localized and located in the mixed layer exclusively. In places where the local Rossby number reaches  $\mathcal{O}(1)$ , geostrophic balance is lost and a vertical secondary ageostrophic circulation begins to slump the isopycnals and restore the flow to a more geostrophically-balanced flow. This ageostrophic secondary circulation therefore generates “hot spots” of higher vertical velocities. The fine-scale structures in the vertical velocity field corresponding to  $\mathcal{O}(1)$  Rossby numbers can be seen in Figure 5, with local vertical velocities up to 60 m/day ( $\sim 7 \times 10^{-4} \text{ m/s}$ ). Contrary to the PDF of relative vorticity, the distribution of vertical velocities demonstrate a negative skewness ( $s = -0.25$ ). This is in agreement with the theory: In fact, positive relative vorticity is associated with the dense side of a density front, where vertical velocities are negative (Mahadevan, 2016). Once again, the amplitude of these vertical velocity hot spots is coherent with the scaling  $w \propto RofU/N$ : using  $Ro \sim 1$ ,  $N \sim 10^{-2} \text{ 1/s}$ ,  $f \sim 10^{-5} \text{ 1/s}$ , and  $U \sim 0.1 \text{ m/s}$ , we obtain  $w \sim 10^{-4} \text{ m/s}$ , or  $\sim 10^1 \text{ m/day}$ .

Comparing *Papa-summer* and *Papa-winter* highlights the different dynamical regimes in the two experiments. In *Papa-winter*, density fronts tend to be sharper, meaning larger density gradients over shorter spatial scales. When computed at the kilometer-scale, the PDF of horizontal buoyancy gradients in *Papa-winter* exhibits a longer tail than in *Papa-summer* (Figure 5). When compared to observations, the PDFs of  $M^2$  in *Papa-summer* and *Papa-winter* demonstrate a correlation with observations of  $r = 0.93$  and  $r = 0.95$ , respectively.

The wider PDF of vertical velocities in *Papa-winter* shows advective velocities that match and exceed typical gravitational sinking velocities, particularly for smaller, and therefore slower-sinking, particulate organic material. The secondary ageostrophic circulation that develops at submeso-scales (i.e.,  $Ro \mathcal{O}(1)$ ) therefore generates an ex-

port mechanism that directly competes with the traditional paradigm that relies on gravitational sinking leading the export of particulate matter in the ocean.

### 3.2 Gravitational and Advective Export of POC

Both model experiments described above were then used to investigate the relationship between ocean dynamics and particle downward flux, using Lagrangian particle-tracking. Domain-averaged, downward particle flux is expected to be a combination of the flux driving by gravitational sinking ( $\langle w_s B \rangle$ ), and by the vertical advective currents affecting the particle along its pathway ( $\langle wB \rangle$ ). The deviation in particle depths from the traditional one-dimensional gravitationally driven model is shown in Figure 6 for both summer and winter cases. In the summer, the PDF of particle density versus depth remains relatively narrow through time, and is centered on a depth level that can be predicted using a simple 1D gravitational model (see shaded curves in Figure 6). The spread in the particle density also vary little among particle classes with different sinking velocities, suggesting that downward fluxes of particles is greatly dominated by gravitational settling and is not subject to significant vertical ocean currents.

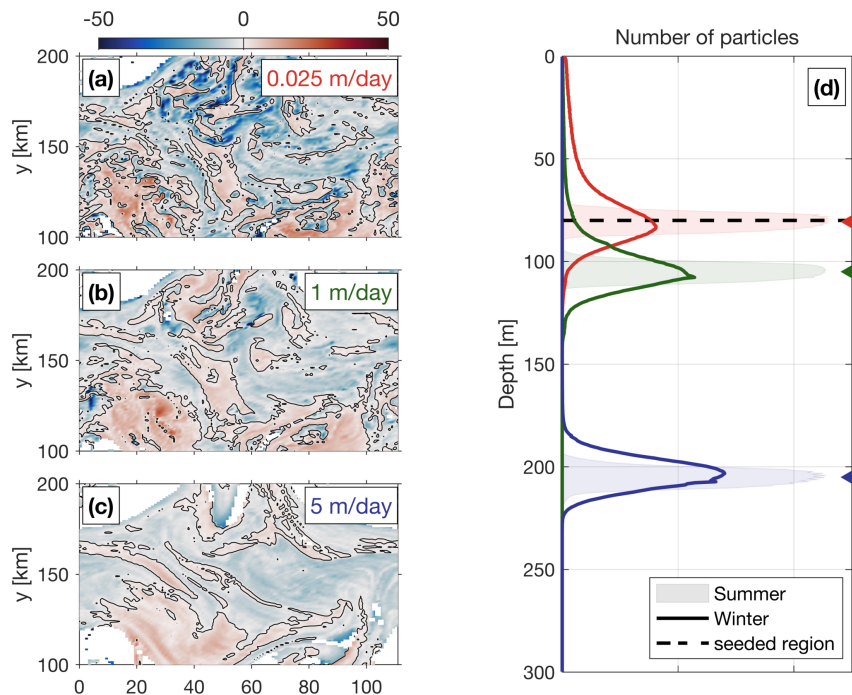


**Figure 6.** [left] The median depth anomaly of particles with a sinking speed (a) 0.025 m/d, (b) 1 m/d, (c) 5 m/d within each grid cell for the winter case 25 days after particles are released. The ‘depth anomaly’ is with respect to the ‘expected’ sinking depth (= sinking speed  $\times$  time since release). Blue (red) grid cells indicate that the median depth of particles in this cell is deeper (shallower) than expected, based on a 1D gravitational model where  $z = w_s \times t$ . [right] (d) Probability Distribution Function (PDF) of particles as a function of depth for each velocity class. The winter distribution is shown as thick lines, while the summer distribution is represented by the shaded regions. Triangle markers indicate the expected depth of particles after 25 days based on the 1D gravitational model, which is used as a reference to compute the depth anomalies. Release depth is indicated by the thick dashed line.

In the winter, however, PDFs of particle density versus depth is wider, in agreement with the stronger vertical ocean currents occurring in the winter (see Figure 5). A top-view of the deviation in the downward particle flux from the traditionally considered 1D gravitational model can be seen in Figure 6 (panels (a)-(c)). Slower-sinking particles deviate more than faster-sinking particles, exhibiting median depth anomalies up to 50 m. This is due to the fact that slower-sinking particles spend more time in the mixed layer, where most of the stronger vertical currents tend to occur (Figure 5). An interesting result emerges from the spatial distribution of the depth-anomaly: both positive (i.e., particles are shallower than expected) and negative (i.e., particles are deeper than expected) anomalies are organized into features with a length-scale  $\mathcal{O}(1\text{-}10 \text{ km})$ . This further highlights the importance of winter submesoscale circulation for vertical fluxes of particles.

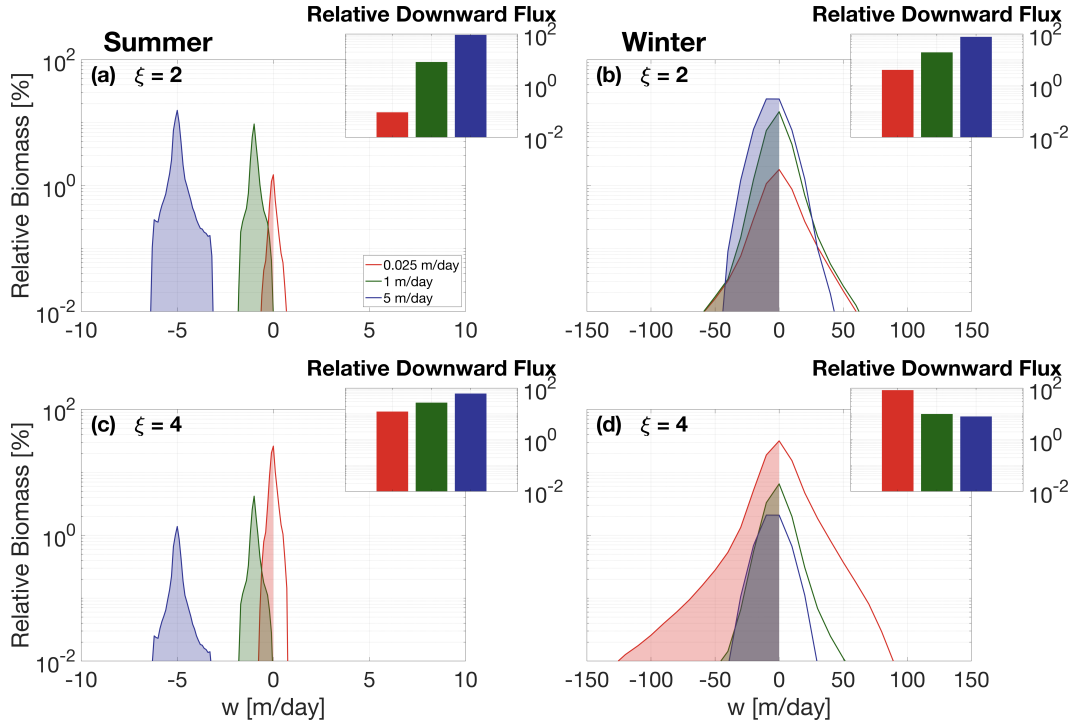
A relative amount of biomass is associated to the particles using Equation (8). PDFs of relative biomass as a function of the vertical velocity is shown in Figure 7. Following the traditional paradigm derived from the simple 1D gravitational model, the downward flux of biomass in the summer is dominated by faster-sinking particle classes capable of carrying particulate material downwards more efficiently. The contribution of slower-sinking particles, however, depends critically on the slope of the size spectrum (see Figure 4). As the Junge slope increases, the spectrum of biomass steepens, and the relative contribution of slower-sinking particles to the downward biomass flux significantly increases (Figure 7c). In fact, the contribution of slower-sinking particles to the summer downward flux increases by a factor 100 (from 0.1% to 10%) when the Junge slope varies from  $\xi = 2$  to  $\xi = 4$ . While significant, the impact of a change in the Junge slope in summer conditions does not challenge the dominant role played by faster-sinking particles. This result can be explained by the fact that, in the summer, vertical velocities are weak and vertical biomass fluxes are therefore gravitationally-driven ( $\langle w_s B \rangle > \langle w B \rangle$ ).

In the winter, PDFs of relative biomass as a function of vertical velocities present a much larger spread, with velocity magnitudes exceeding 50 m/day. For  $\xi = 2$ , the relative contribution of slower-sinking particles to the downward flux significantly increases from 0.1% in the summer to about 4% in the winter, demonstrating the impact advective velocities alone can have on vertical fluxes (Figure 7b). Nevertheless, slower-sinking particles remain a relatively small contributor to the total downward flux of biomass. When winter ocean dynamics are coupled with a steeper Junge slope, however, slower-sinking particles largely dominate the downward biomass flux. In our winter simulations with  $\xi = 4$ , we find that the slowest-sinking particle class is responsible for about 80% of the biomass flux (Figure 7d).

Our results show that both a steepening of the particle size spectrum and the presence of submesoscale dynamics can enhance the contribution of slower-sinking particles to the downward biomass flux. While the former is simply due to an increase in particle density in slower-sinking particle classes, the latter is attributed to the larger vertical velocity generated by submesoscale instabilities. When both are combined, as expected in the wintertime, slower-sinking particles then become the leading contributor to the downward biomass transport. However, slower-sinking particles are generally expected to remineralize on timescales shorter than their export timescale, fueling the argument that the focus should be upon faster-sinking particle classes. The impacts of remineralization on export are thus considered in the following section to test the robustness of the findings.

### 3.3 Particle Remineralization

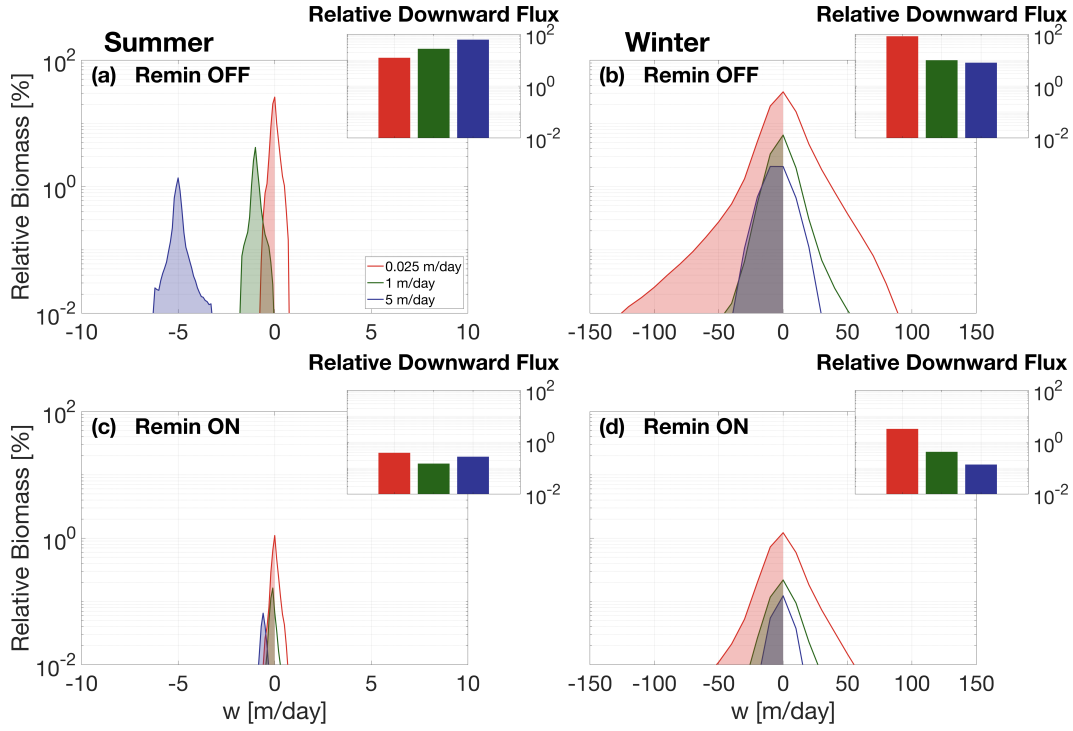
Both submesoscale dynamics and the Junge slope were identified as key factors impacting the respective role played by different particle classes in driving downward



481 **Figure 7.** Probability Distribution Function (PDF) of relative biomass versus vertical velocity  
 482 along particle trajectories in the summer case [left] and winter case [right], with a Junge slope  
 483 of 2 [top] and 4 [bottom]. Inserts show the integrated relative downward biomass flux associated  
 484 with each sinking-velocity class. Both winter dynamics and steeper Junge slopes tend to increase  
 485 the relative contribution of slower-sinking particles.

510 biomass fluxes. Simple Lagrangian particles were used to isolate the effects of these  
 511 two factors. In reality, however, sinking velocities of particulate matter varies in time  
 512 as the particles slowly remineralize. A remineralizing behavior was therefore imple-  
 513 mented for the Lagrangian particles, using Equation (10), to investigate the impact  
 514 that remineralization processes have on our findings. The traditional paradigm relies  
 515 on the fact that slow-sinking particles tend to fully remineralize over short timescales,  
 516 further enhancing the importance of faster-sinking particles classes in driving down-  
 517 ward biomass fluxes. While this paradigm holds for flatter Junge slope, where the  
 518 biomass content is dominated by faster-sinking particles, it becomes unfit at steeper  
 519 slopes.

520 Figure 8 compares the relative biomass and downward biomass fluxes associated  
 521 with each of the modeled particle classes for  $\xi = 4$  with and without the remineral-  
 522 ization scheme. As previously detailed, downward fluxes of biomass are dominated  
 523 by faster-sinking particles during summertime and in the absence of remineralization.  
 524 This is due to the fact that the flux of biomass  $\langle w_{tot}B \rangle = \langle w_s B \rangle + \langle w B \rangle$  is driven by  
 525  $\langle w_s B \rangle$ , despite a smaller relative biomass content per particle. This is characteristic  
 526 of a gravitationally-driven system, where settling velocity dictates the contribution to  
 527 downward fluxes. Implementing remineralization processes, however, directly affects  
 528 the particle settling velocity which slows down as particles remineralize. This effect  
 529 can be seen in Figure 8c, where PDFs of relative biomass per particle class are shifted  
 530 towards weaker vertical velocities than in the absence of remineralization, as predicted  
 531 by Equation (10). As a result, the gravitationally-driven term  $\langle w_s B \rangle$  decreases with



534 **Figure 8.** Probability Distribution Function (PDF) of relative biomass versus vertical ve-  
 535 locity along particle trajectories in the summer case [left] and winter case [right], ignoring [top]  
 536 and including [bottom] particle remineralization, for  $\xi = 4$  and 25 days after particle release.  
 537 Inserts show the integrated relative downward biomass flux associated with each sinking-velocity  
 538 class. Remineralization processes have the greatest impact on fast-sinking particles, especially in  
 539 summer dynamics.

532 time, and the downward flux of biomass becomes generally advectively-driven by day  
 533 25 (Figure 8).

540 In an advectively-driven system where  $\langle w_s B \rangle < \langle w B \rangle$ , the relative amount of  
 541 biomass content in a particle class becomes important and dictates the respective con-  
 542 tribution of each particle class to the total downward biomass fluxes. This shift from a  
 543 gravitationally-driven to an advectively-driven system is observed when implementing  
 544 particle remineralization in the summer (Figure 8c): in the absence of remineralization,  
 545 faster-sinking particles dominate the downward biomass fluxes (60%; see Figure 8a).  
 546 When remineralization processes are considered, slower-sinking particles become the  
 547 dominant contributor to biomass fluxes (see inset in Figure 8c). As shown in Figure  
 548 7, downward biomass fluxes in the wintertime are generally advectively-driven, due  
 549 to the larger vertical velocities associated with wintertime ocean dynamics. Biomass  
 550 fluxes are dominated by the slower-sinking particles, representing 82% of the down-  
 551 ward biomass flux (Figure 8b). Even after implementing our remineralization scheme,  
 552 slower-sinking particles remain the largest contributor to downward biomass fluxes  
 553 (87%; see Figure 8d).

554 These results highlight the importance in considering slower-sinking particle  
 555 classes when considering downward biomass fluxes. It also demonstrates that, con-  
 556 trarily to the traditional paradigm, remineralization processes enhance the role played  
 557 by slower-sinking particles in biomass fluxes, in cases where the biomass spectrum  
 558 slope is negative.

559 The timescales over which the system transitioned from an gravitationally-driven  
 560 to an advectively-driven system depends on the remineralization model used.

## 561 4 Discussion

### 562 4.1 Dynamical Regimes

563 *Papa-summer* and *Papa-winter* experiments were designed to statistically cap-  
 564 ture the ocean dynamics at Station Papa (145°W, 50°N) in the Northeast Pacific  
 565 Ocean. After spin-up, the model demonstrated similar distributions of both horizontal  
 566 ( $M^2$ ) and vertical ( $N^2$ ) density gradients to observational estimates from underwater  
 567 gliders (see Figures 2, 3, and 5). The two experiments, however, show significantly  
 568 different distributions of  $M^2$ , with the winter distribution exhibiting a longer tail, due  
 569 to sharper density gradients. The tail of the wintertime distribution is only partially  
 570 captured by the glider data, due to the fact that underwater gliders sampled gradients  
 571 at spatial scales of 10 km and greater, while the model has a horizontal resolution of  
 572 500 m, allowing sharper submesoscale fronts and filaments to be formed.

573 Studies investigating submesoscale dynamics traditionally focused on regions  
 574 where the presence of submesoscale fronts and filaments are established, such as west-  
 575 ern boundary currents with strong gradients (D'Asaro, Lee, Rainville, Harcourt, &  
 576 Thomas, 2011; Thomas, Tandon, & Mahadevan, 2013), or the edge of mesoscale fea-  
 577 tures (van Haren et al., 2006; Waite et al., 2016). The seasonality in submesoscale  
 578 dynamics captured in the glider dataset at Station Papa and reflected in the model  
 579 experiments, echoes the behavior seen from recent observational studies conducted  
 580 at a similar latitude in the Atlantic Ocean, which demonstrate the intensification of  
 581 submesoscale dynamics in the wintertime (Buckingham et al., 2016; Thompson et al.,  
 582 2016). Despite being sometimes qualified as an “eddy desert” with low kinetic energy  
 583 (Chelton, Schlax, & Samelson, 2011), ocean characteristics in the eastern part of the  
 584 Pacific subpolar gyre suggest the presence of submesoscale features in the wintertime:  
 585 strong density gradients, localized Rossby numbers of order 1, a balanced Richardson  
 586 number  $Rib = \frac{f^2 N^2}{M^4}$  smaller than 1, a positively skewed distribution in vorticity, and a  
 587 negatively skewed distribution of vertical velocities (see Figure 5; Buckingham et al.,  
 588 2016; Rudnick, 2001; Thomas, Taylor, et al., 2013).

589 Strong downward velocities are hypothesized to enhance POC export by advect-  
 590 ing slower-sinking particles out of the mixed layer. *Papa-winter* indeed exhibits vertical  
 591 velocities more than 20 times larger than in *Papa-summer*. The vertical currents in  
 592 *Papa-winter*, however, tend to be much patchier than the weaker vertical currents  
 593 observed in *Papa-summer*. Because both particle production and downward vertical  
 594 velocities present a high degree of patchiness, it requires a certain level of covariance  
 595 between the two fields for the export to effectively be enhanced (Mahadevan et al.,  
 596 2012). A more realistic seeding strategy for Lagrangian particles, such as one guided  
 597 by biological tracers, would likely provide important information towards a better  
 598 understanding of the effects of patchiness on POC export at submeso-scales

599 The hypothesis tested in this study is that submesoscale activity enhances export  
 600 of particulate matter at Station Papa by shortening the export timescale of particulate  
 601 matter. The wintertime intensification in submesoscale activity has the potential to  
 602 indeed enhance export (see discussion in Section 4.2). However, the seasonal cycle  
 603 in submesoscale activity is out of phase with the one in net community productivity,  
 604 which peaks in the spring and summertime when the mixed layer is shallower (Plant  
 605 et al., 2016). Two mechanisms are therefore present to potentially sustain a year-long  
 606 POC export flux: In the winter, less particulate material is present in the mixed layer,  
 607 but active submesoscale dynamics tend to enhance the POC export flux by advecting  
 608 the more numerous slower-sinking particles into the ocean interior. In the summer,

609 the production of POC is at its yearly maximum, but export tends to be dominated  
 610 by gravitational sinking, which favors faster-sinking particles and thus exclude part of  
 611 the particle spectrum from contributing to the export flux.

## 612 4.2 Downward Fluxes

613 Analyses of particle tracking experiments reveal that the contribution of slower-  
 614 sinking particles to the downward particulate flux depends on two main factors: (1)  
 615 the dynamics of the oceanic flow field, and (2) the slope of the size spectrum (i.e., the  
 616 Junge slope  $\xi$ ).

617 Mixed layer ocean dynamics at station Papa change significantly between the  
 618 winter and the summer. In the winter, submesoscale dynamics are intensified, and  
 619 sharp fronts and filaments develop in the mixed layer. This seasonal change in dy-  
 620 namics is consistent with recent observations (Buckingham et al., 2016; Thompson  
 621 et al., 2016), and models (Brannigan, Marshall, Naveira-Garabato, & George Nurser,  
 622 2015; Callies et al., 2015; Rocha, Gille, Chereskin, & Menemenlis, 2016) characterizing  
 623 the seasonal cycle of submesoscale dynamics. The winter intensification in subme-  
 624 soscale dynamics was proven to have an important impact on the downward flux of all  
 625 sinking-velocity classes modeled in this experiment.

626 In the summer, gravitational sinking governs a downward particulate flux, which  
 627 is dominated by faster-sinking particles, with little to no contribution from slower-  
 628 sinking particles. In the winter, however, vertical fluxes tend to be advectively-driven,  
 629 which leads to a slightly weaker downward flux of faster-sinking particles than in the  
 630 summer due to resuspension, but a much larger flux of slower-sinking particles, which  
 631 are present in far greater numbers (Figure 7). The gravitationally-driven flux in the  
 632 summer is mechanistically different from the advectively-driven winter flux, which  
 633 raises the question as to which process is most efficient in driving a downward flux of  
 634 particulate material.

635 In the absence of remineralization, both a steeper size spectrum slope ( $\xi > 3$  in  
 636 this case) and enhanced submesoscale dynamics, increase the contribution of slower-  
 637 sinking particle classes to the downward biomass flux. This is only when both of  
 638 these conditions are combined, however, that slower-sinking particles dominate the  
 639 downward flux of biomass (Figure 7). This is a significant result, as Junge slopes  
 640 greater than 3 have been observed in the ocean (Kostadinov, Siegel, & Maritorena,  
 641 2009; White et al., 2015). The threshold value of  $\xi = 3$  for a change in the biomass  
 642 spectral slope (see Figure 4b) is of course a consequence of first-order approximations  
 643 used in this study describing the relationships between particle size, sinking veloc-  
 644 ity, and biomass content. Nevertheless, our results demonstrate the importance of  
 645 including the smaller particle size range of the particle spectrum, in the estimation or  
 646 measurement of vertical fluxes, especially when submesoscale dynamics are active. It  
 647 also highlights the importance of better constraining the relationships linking particle  
 648 size, sinking velocity, and biomass content.

649 Introducing remineralization processes significantly decreases the biomass flux.  
 650 Counter-intuitively, however, the implementation of a remineralization scheme further  
 651 strengthens the contribution of slower-sinking particles to the biomass flux (Figure  
 652 8). This can be explained by the fact that remineralization processes have a greater  
 653 impact on sinking-velocity classes that rely on gravitational sinking to be exported, as  
 654 these particles decelerate as they remineralize. In the summer, all particle classes are  
 655 similarly affected by remineralization, as downward fluxes are gravitationally-driven.  
 656 In the winter, however, slower-sinking particles are exported through advective pro-  
 657 cesses. Their export timescale is barely affected by remineralization processes as it  
 658 only depends on local ocean dynamics.

The results of this study suggest that slow- and non-sinking particles must be considered when studying the downward flux of particulate matter in the upper ocean. The patchiness associated with both particle production and submesoscale features poses a real observational challenge to properly resolve vertical fluxes. Based on our findings, subsequent studies should focus on testing the impact of patchiness on vertical fluxes. In the wintertime, when size spectral slope is steep and submesoscale dynamics most active, vertical fluxes could be grossly underestimated depending on the level of co-occurrence between particle production and stronger vertical currents.

## 5 Conclusion

The main conclusions of this study are:

1. Ocean dynamics in the subpolar Northeast Pacific exhibit a seasonal cycle with low submesoscale activity in the summertime, and more submesoscale features present in the wintertime. Submesoscale dynamics generate larger, and asymmetric, vertical currents leading to a vertical biomass flux driven by advective processes, as opposed to gravitational sinking in the summertime.
2. Submesoscale dynamics generally enhance the downward particulate flux by increasing the contribution of slower-sinking particles to the total flux through advective transport. The slower-sinking particles are found to be significant for export, and can be even make the dominant contribution under certain conditions.
3. The contribution of slower-sinking particles to the downward biomass flux depends on the slope of the particle size spectra (i.e., the Junge Slope), that controls the relative number of particles per size class. Two cases emerge from this study:
  - (a) If the Junge slope is smaller than 3, larger particles contribute most to vertical biomass fluxes independently of flow dynamics, as there are no mechanisms capable of selectively advecting slower-sinking particles. The system is described as gravitationally-driven.
  - (b) If the Junge slope is greater than 3, as most commonly observed, ocean dynamics become key for determining which particle classes dominate the downward flux. As submesoscale dynamics become more active, ageostrophic circulations leading to larger vertical velocities develop. In these conditions, downward biomass fluxes are largely driven by the slower-sinking particle classes.
4. Remineralization processes logically reduce the amount of biomass flux. However, it unexpectedly enhances the role of slower-sinking particles, which are advectively transported. The impact of remineralization is greater on faster-sinking particles since it affects both the biomass content and their sinking velocity.

## Acknowledgments

The work was funded by NASA grant NNX16AR48G, to complement the EXPORT Processes in the global Ocean from RemoTe Sensing (EXPORTS) program. We would like to thank A. Thompson (Caltech) for his useful comments and suggestions, N. Pelland (NOAA) and Charlie Eriksen (University of Washington) for sharing the glider data collected at Ocean Station Papa, as well as Sebastian Essink for his assistance in developing the particle-tracking code. All data used in this manuscript are publicly available: Ocean Station Papa data is available on PMEL's website (<https://www.pmel.noaa.gov/ocs/Papa>; Laboratory, 2018) and gridded Argo products can be downloaded at <http://www.seanoe.org/data/00348/45945> (Gaillard,

708 2015). Glider data is archived at the University of Washington's Library (<http://hdl.handle.net/1773/41656>; Pelland, 2018).

## 710 References

- 711 Alkire, M., D'Asaro, E., Lee, C., Perry, M., Gray, A., Cetinic, I., ... González-  
 712 Posada, A. (2012). Estimates of net community production and export using  
 713 high-resolution, Lagrangian measurements of O<sub>2</sub>, NO<sub>3</sub><sup>-</sup>, and POC through the  
 714 evolution of a spring diatom bloom in the North Atlantic. *Deep-Sea Res. I*,  
 715 64, 157-174. doi: 10.1016/j.dsr.2012.01.012
- 716 Bach, L. T., Riebesell, U., Sett, S., Febiri, S., Rzepka, P., & Schulz, K. G. (2012).  
 717 An approach for particle sinking velocity measurements in the 3400 μm size  
 718 range and considerations on the effect of temperature on sinking rates. *Marine  
 719 Biology*, 159(8), 1853–1864. doi: 10.1007/s00227-012-1945-2
- 720 Bower, A. S., & Rossby, T. (1989). Evidence of Cross-Frontal Exchange Processes  
 721 in the Gulf Stream Based on Isopycnal RAFOS Float Data. *Journal of Phys-  
 722 ical Oceanography*, 19(9), 1177–1190. doi: 10.1175/1520-0485(1989)019<1177:  
 723 EOCFEP>2.0.CO;2
- 724 Brannigan, L., Marshall, D. P., Naveira-Garabato, A., & George Nurser, A. (2015).  
 725 The seasonal cycle of submesoscale flows. *Ocean Modelling*, 92, 69–84. doi: 10  
 726 .1016/j.ocemod.2015.05.002
- 727 Briggs, N., Perry, M. J., Cetini, I., Lee, C., D'Asaro, E., Gray, A. M., & Rehm, E.  
 728 (2011). High-resolution observations of aggregate flux during a sub-polar north  
 729 atlantic spring bloom. *Deep Sea Research Part I: Oceanographic Research  
 730 Papers*, 58(10), 1031 - 1039. doi: 10.1016/j.dsr.2011.07.007
- 731 Buckingham, C. E., Naveira Garabato, A. C., Thompson, A. F., Brannigan, L.,  
 732 Lazar, A., Marshall, D. P., ... Belcher, S. E. (2016). Seasonality of sub-  
 733 mesoscale flows in the ocean surface boundary layer. *Geophysical Research  
 734 Letters*, 43(5), 2118–2126. doi: 10.1002/2016GL068009
- 735 Callies, J., Ferrari, R., Klymak, J. M., & Gula, J. (2015). Seasonality in sub-  
 736 mesoscale turbulence. *Nature communications*, 6, 6862. doi: 10.1038/  
 737 ncomms7862
- 738 Chelton, D. B., Schlax, M. G., & Samelson, R. M. (2011). Global observations of  
 739 nonlinear mesoscale eddies. *Progress in Oceanography*, 91(2), 167–216. doi: 10  
 740 .1016/j.pocean.2011.01.002
- 741 D'Asaro, E., Lee, C., Rainville, L., Harcourt, R., & Thomas, L. (2011). Enhanced  
 742 turbulence and energy dissipation at ocean fronts. *Science*, 332(6027), 318–  
 743 322. doi: 10.1126/science.1201515
- 744 Döös, K., Kjellsson, J., & Jönsson, B. (2013). TRACMASS – A Lagrangian Trajec-  
 745 tory Model. In *Preventive methods for coastal protection* (pp. 225–249). Heidel-  
 746 berg: Springer International Publishing. doi: 10.1007/978-3-319-00440-2\_7
- 747 Estapa, M. L., Siegel, D. A., Buesseler, K. O., Stanley, R. H. R., Lomas, M. W., &  
 748 Nelson, N. B. (2015). Decoupling of net community and export production  
 749 on submesoscales in the Sargasso Sea. *Global Biogeochemical Cycles*, 29(8),  
 750 1266–1282. doi: 10.1002/2014GB004913
- 751 Falkowski, P. G., Barber, R. T., & Smetacek, V. (1998). Biogeochemical Controls  
 752 and Feedbacks on Ocean Primary Production. *Science*, 281(5374), 200–206.  
 753 doi: 10.1126/science.281.5374.200
- 754 Fox-Kemper, B., Ferrari, R., & Hallberg, R. (2008). Parameterization of Mixed  
 755 Layer Eddies. Part I: Theory and Diagnosis. *Journal of Physical Oceanogra-  
 756 phy*, 38(6), 1145–1165. doi: 10.1175/2007JPO3792.1
- 757 Gaillard, F. (2015). ISAS-13 temperature and salinity gridded fields. SEANOE. doi:  
 758 10.17882/45945
- 759 Gaillard, F., Reynaud, T., Thierry, V., Kolodziejczyk, N., & von Schuckmann, K.  
 760 (2016). In situ-based reanalysis of the global ocean temperature and salinity

- 761 with isas: Variability of the heat content and steric height. *Journal of Climate*,  
 762 29(4), 1305–1323. doi: 10.1175/JCLI-D-15-0028.1
- 763 Gruber, N., Lachkar, Z., Frenzel, H., Marchesiello, P., Münnich, M., McWilliams,  
 764 J. C., ... Plattner, G.-K. (2011). Eddy-induced reduction of biological pro-  
 765 duction in eastern boundary upwelling systems. *Nature geoscience*, 4(11), 787.  
 766 doi: 10.1038/NGEO1273
- 767 Harrison, P. J., Whitney, F. A., Tsuda, A., Saito, H., & Tadokoro, K. (2004).  
 768 Nutrient and Plankton Dynamics in the NE and NW Gyres of the Sub-  
 769 arctic Pacific Ocean. *Journal of Oceanography*, 60(1), 93–117. doi:  
 770 10.1023/B:JOCE.0000038321.57391.2a
- 771 Hoskins, B. J., & Bretherton, F. P. (1972). Atmospheric Frontogenesis Models:  
 772 Mathematical Formulation and Solution. *Journal of the Atmospheric Sciences*,  
 773 29(1), 11–37. doi: 10.1175/1520-0469(1972)029<0011:AFMMFA>2.0.CO;2
- 774 Iversen, M. H., & Ploug, H. (2010). Ballast minerals and the sinking carbon flux in  
 775 the ocean: carbon-specific respiration rates and sinking velocity of marine snow  
 776 aggregates. *Biogeosciences*, 7(9), 2613–2624. doi: 10.5194/bg-7-2613-2010
- 777 Iversen, M. H., & Ploug, H. (2013). Temperature effects on carbon-specific respi-  
 778 ration rate and sinking velocity of diatom aggregates - potential implications  
 779 for deep ocean export processes. *Biogeosciences*, 10(6), 4073–4085. doi:  
 780 10.5194/bg-10-4073-2013
- 781 Klein, P., & Lapeyre, G. (2009). The Oceanic Vertical Pump Induced by Mesoscale  
 782 and Submesoscale Turbulence. *Annual Review of Marine Science*, 1(1), 351–  
 783 375. doi: 10.1146/annurev.marine.010908.163704
- 784 Kostadinov, T. S., Siegel, D. A., & Maritorena, S. (2009). Retrieval of the particle  
 785 size distribution from satellite ocean color observations. *Journal of Geophysical  
 786 Research*, 114(C9), C09015. doi: 10.1029/2009JC005303
- 787 Laboratory, P. M. E. (2018). *Ocean Climate Stations Mooring Data*. Retrieved from  
 788 <https://www.pmel.noaa.gov/ocs/data-overview>
- 789 Lévy, M., Ferrari, R., Franks, P. J. S., Martin, A. P., & Rivière, P. (2012). Bringing  
 790 physics to life at the submesoscale. *Geophysical Research Letters*, 39(14), n/a–  
 791 n/a. doi: 10.1029/2012GL052756
- 792 Lévy, M., Klein, P., & Treguier, A.-M. (2001). Impact of sub-mesoscale physics on  
 793 production and subduction of phytoplankton in an oligotrophic regime. *Jour-  
 794 nal of marine research*, 59(4), 535–565. doi: 10.1357/002224001762842181
- 795 Mahadevan, A. (2016). The Impact of Submesoscale Physics on Primary Produc-  
 796 tivity of Plankton. *Annual Review of Marine Science*, 8(1), 161–184. doi: 10  
 797 .1146/annurev-marine-010814-015912
- 798 Mahadevan, A., & Archer, D. (2000). Modeling the impact of fronts and  
 799 mesoscale circulation on the nutrient supply and biogeochemistry of the up-  
 800 per ocean. *Journal of Geophysical Research: Oceans*, 105(C1), 1209–1225. doi:  
 801 10.1029/1999JC900216
- 802 Mahadevan, A., D'Asaro, E., Lee, C., & Perry, M. J. (2012). Eddy-Driven Strat-  
 803 ification Initiates North Atlantic Spring Phytoplankton Blooms. *Science*,  
 804 337(6090), 54–58. doi: 10.1126/science.1218740
- 805 Mahadevan, A., Olinger, J., & Street, R. (1996a). A Nonhydrostatic Mesoscale Ocean  
 806 Model. Part II: Numerical Implementation. *Journal of Physical Oceanography*,  
 807 26(9), 1881–1900. doi: 10.1175/1520-0485(1996)026<1881:ANMOMP>2.0.CO;  
 808 2
- 809 Mahadevan, A., Olinger, J., & Street, R. (1996b). A Nonhydrostatic mesoscale ocean  
 810 model. Part I: Well-posedness and scaling. *Journal of Physical Oceanography*,  
 811 26(9), 1868–1880. doi: 10.1175/1520-0485(1996)026<1868:ANMOMP>2.0.CO;  
 812 2
- 813 Mahadevan, A., & Tandon, A. (2006). An analysis of mechanisms for submesoscale  
 814 vertical motion at ocean fronts. *Ocean Modelling*, 14(3-4), 241–256. doi: 10  
 815 .1016/J.OCEMOD.2006.05.006

- 816 McDonnell, A. M. P., & Buesseler, K. O. (2010). Variability in the average sinking  
 817 velocity of marine particles. *Limnology and Oceanography*, 55(5), 2085–2096.  
 818 doi: 10.4319/lo.2010.55.5.2085
- 819 McWilliams, J. C. (2016). Submesoscale currents in the ocean. *Proceedings of the  
 820 Royal Society A: Mathematical, Physical and Engineering Science*, 472(2189).  
 821 doi: 10.1098/rspa.2016.0117
- 822 Mensa, J. A., Garraffo, Z., Griffa, A., Özgökmen, T. M., Haza, A., & Veneziani, M.  
 823 (2013). Seasonality of the submesoscale dynamics in the Gulf Stream region.  
 824 *Ocean Dynamics*, 63(8), 923–941. doi: 10.1007/s10236-013-0633-1
- 825 Mesinger, F., DiMego, G., Kalnay, E., Mitchell, K., Shafran, P. C., Ebisuzaki, W.,  
 826 ... Shi, W. (2006). North american regional reanalysis. *Bulletin of the Ameri-  
 827 can Meteorological Society*, 87(3), 343–360. doi: 10.1175/BAMS-87-3-343
- 828 Omand, M. M., D'Asaro, E. A., Lee, C. M., Perry, M. J., Briggs, N., Cetini, I.,  
 829 & Mahadevan, A. (2015). Eddy-driven subduction exports particulate or-  
 830 ganic carbon from the spring bloom. *Science*, 348(6231), 222–225. doi:  
 831 10.1126/science.1260062
- 832 Pelland, N. (2018). *Seaglider Surveys at Ocean Station Papa: Bin-Averaged Profiles,  
 833 Currents, and Independent Oxygen Data*. Retrieved from <http://hdl.handle.net/1773/41656>
- 834 Pelland, N., Eriksen, C., & Cronin, M. (2016). Seaglider surveys at Ocean Station  
 835 Papa: Circulation and watermass properties in a meander of the North Pa-  
 836 cific Current. *Journal of Geophysical Research: Oceans*, 121, 6816–6846. doi:  
 837 10.1002/2016JC011920
- 838 Plant, J. N., Johnson, K. S., Sakamoto, C. M., Jannasch, H. W., Coletti, L. J.,  
 839 Riser, S. C., & Swift, D. D. (2016). Net community production at Ocean Sta-  
 840 tion Papa observed with nitrate and oxygen sensors on profiling floats. *Global  
 841 Biogeochemical Cycles*, 30(6), 859–879. doi: 10.1002/2015GB005349
- 842 Ploug, H., Iversen, M. H., Koski, M., & Buitenhuis, E. T. (2008). Production,  
 843 oxygen respiration rates, and sinking velocity of copepod fecal pellets: Direct  
 844 measurements of ballasting by opal and calcite. *Limnology and Oceanography*,  
 845 53(2), 469–476. doi: 10.4319/lo.2008.53.2.0469
- 846 Rocha, C. B., Gille, S. T., Chereskin, T. K., & Menemenlis, D. (2016). Seasonal-  
 847 ity of submesoscale dynamics in the Kuroshio Extension. *Geophysical Research  
 848 Letters*, 43(21), 11,304–11,311. doi: 10.1002/2016GL071349
- 849 Rudnick, D. L. (2001). On the skewness of vorticity in the upper ocean. *Geophysical  
 850 Research Letters*, 28(10), 2045–2048. doi: 10.1029/2000GL012265
- 851 Sheldon, R., Prakash, A., & Sutcliffe, W., Jr. (1972). The size distribution of parti-  
 852 cles in the ocean. *Limnology and Oceanography*, 17(3), 327–340. doi: 10.4319/  
 853 lo.1972.17.3.0327
- 854 Sherry, N. D., Boyd, P. W., Sugimoto, K., & Harrison, P. J. (1999). Seasonal and  
 855 spatial patterns of heterotrophic bacterial production, respiration, and biomass  
 856 in the subarctic NE Pacific. *Deep-Sea Research Part II: Topical Studies in  
 857 Oceanography*, 46(11-12), 2557–2578. doi: 10.1016/S0967-0645(99)00076-4
- 858 Thomas, L. N., Tandon, A., & Mahadevan, A. (2013). Submesoscale processes and  
 859 dynamics. In *Ocean modeling in an eddying regime* (p. 17–38). American Geo-  
 860 physical Union (AGU). doi: 10.1029/177GM04
- 861 Thomas, L. N., Taylor, J. R., Ferrari, R., & Joyce, T. M. (2013). Symmetric in-  
 862 stability in the Gulf Stream. *Deep Sea Research Part II: Topical Studies in  
 863 Oceanography*, 91, 96–110. doi: 10.1016/j.dsr2.2013.02.025
- 864 Thompson, A. F., Lazar, A., Buckingham, C., Naveira Garabato, A. C., Damerell,  
 865 G. M., & Heywood, K. J. (2016). Open-Ocean Submesoscale Motions: A Full  
 866 Seasonal Cycle of Mixed Layer Instabilities from Gliders. *Journal of Physical  
 867 Oceanography*, 46(4), 1285–1307. doi: 10.1175/JPO-D-15-0170.1
- 868 van Haren, H., Millot, C., & Taupier-Letage, I. (2006). Fast deep sinking in Mediter-  
 869 ranean eddies. *Geophysical Research Letters*, 33(4), L04606. doi: 10.1029/  
 870

- 871 2005GL025367  
872 Waite, A. M., Stemmann, L., Guidi, L., Calil, P. H. R., Hogg, A. M. C., Feng, M.,  
873 ... Gorsky, G. (2016). The wineglass effect shapes particle export to the deep  
874 ocean in mesoscale eddies. *Geophysical Research Letters*, 43(18), 9791–9800.  
875 doi: 10.1002/2015GL066463  
876 White, A. E., Letelier, R. M., Whitmire, A. L., Barone, B., Bidigare, R. R., Church,  
877 M. J., & Karl, D. M. (2015). Phenology of particle size distributions  
878 and primary productivity in the North Pacific subtropical gyre (Station  
879 ALOHA). *Journal of Geophysical Research: Oceans*, 120(11), 7381–7399.  
880 doi: 10.1002/2015JC010897